Gao et al. Nanoscale Research Letters (2017) 12:377
DOI 10.1186/s11671-017-2157-y

Nanoscale Research Letters

NANO EXPRESS Open Access

Facile Synthesis of Heterostructured WS_2/Bi_2MoO_6 as High-Performance Visible-Light-Driven Photocatalysts

Jiyun Gao[1,2,3,4], Chenhui Liu[1,2,3,4], Fang Wang[1,2,3,4], Lijuan Jia[1,2,3,4], Kaijiao Duan[1,2,3,4] and Tiancheng Liu[1,2,3,4*]

Abstract

In this paper, novel WS_2/Bi_2MoO_6 heterostructured photocatalysts were successfully fabricated via a facile solvothermal growth method using pre-exfoliated layered WS_2 nanoslices as a substrate. The structure, morphology, and optical properties of the as-prepared WS_2/Bi_2MoO_6 samples were characterized by XRD, XPS, SEM, TEM (HRTEM), and UV-vis diffuse reflectance spectra (DRS). Results confirmed the existence of an excellent nanojunction interface between layered WS_2 nanoslices and Bi_2MoO_6 nanoflakes. Under visible light (>420 nm), the WS_2/Bi_2MoO_6 composites exhibit significantly enhanced photocatalytic activity compared with pure Bi_2MoO_6 toward the decomposition of rhodamine B (RhB). Meanwhile, the active species trapping experiments indicated that holes (h^+) were the main active species during the photocatalytic reaction. The enhanced photocatalytic performance can be ascribed to the effective light harvesting, fast photogenerated electron–hole pairs separation, and excellent charge carrier transport of the WS_2/Bi_2MoO_6 heterostructures. Moreover, the prepared WS_2/Bi_2MoO_6 composites also show good structural and activity stability in repeatability experiments.

Keywords: WS_2/Bi_2MoO_6, Solvothermal, Heterostructure, Visible-light driven, Photocatalysis

Background

The photocatalysis is widely regarded as one of the most promising environmental remediation technique due to the clean energy utilization method [1, 2]. Generally, some accepted that high-efficient photocatalysts with wide forbidden gap, such as TiO_2 and ZnO, can only utilize ultraviolet light irradiation [3]. As to practical application, photocatalysis strategy will be a huge boost once a photocatalyst can favorably absorb the abundant solar energy in visible region. For this purpose, many attempts to probe visible-light photocatalyst for sufficient solar energy utilization by using the narrow band semiconductor [4–6]. Despite the single-phase photocatalyst can be excited smoothly by visible light, it still manifests low energy conversion efficiency due to poor charge separation efficiency resulting from rapid recombination of photo-induced electrons and holes [7]. It is widely accepted that the heterostructure can improve the separation probability of light-induced charge because the contact interfacial region of heterojunction will provide an internal electric field to restrain the recombination probability, thus resulting in an efficient photocatalytic performance. In general, the designed heterostructure will adopt at least one narrow band semiconductor to harvest more visual-light energy and then to generate more photo-induced charges [8, 9].

As a novel photocatalyst, Bi_2MoO_6 has received attention in the field of visual-light-driven photocatalysis because it possesses distinct sandwiched layered structure [10, 11]. As previously mentioned, the pure Bi_2MoO_6 is not suitable for the utilization as an efficient visible-light photocatalyst due to the high recombination probability of photogenerated charge carrier. Therefore, some effective strategies to meet this challenge by using the architecture of proper hybrid nanostructure and especially the introduction of two dimensional (2D) nanosheets have been proved as an effectual approach to strengthen interfacial charge transfer between two components in the process of photocatalytic reaction. Obviously, it is anticipated that

* Correspondence: liutiancheng76@163.com
[1]Joint Research Centre for International Cross-border Ethnic Regions Biomass Clean Utilization in Yunnan, Kunming 650500, China
[2]Education Department of Yunnan, Key Laboratory of Resource Clean Conversion in Ethnic Region, Kunming 650500, China
Full list of author information is available at the end of the article

the heterostructure between Bi_2MoO_6 and 2D layered material will increase photocatalytic efficiency by visual-light irradiation [8].

Layered transition metal dichalcogenides (TMDs) are widely regarded as a kind of promising loading material because of their analogous graphene reticular structure [12, 13]. Especially, monolayer and few layers of TMDs have important application for catalysis and energy storage due to their distinct electronic properties and high specific surface areas [14, 15]. For example, monolayered and few-layer MoS_2 have recently paid the attention of the scientific community in photocatalysis research, which ascribes the lack of interlayer coupling and the absence of inversion symmetry resulting in the photoelectric property that differ markedly from those of the bulk [14, 16, 17]. From the material design perspective for an efficient visible-light-driven sensitized heterojunctional photocatalyst, the primary concern is that the hybrid narrow band gaps (1.1–1.7 eV) can closely match the solar spectrum [18]. In fact, the typical 2D layered semiconductors, such as MoS_2 or g-C_3N_4, have received significant attention to explore potential photocatalysis applications, which lead to TMD nanosheet which is often utilized as a supporter to establish the heterostructured composite photocatalysts via different energy band hybrid strategies [19, 20]. For instance, the hierarchical MoS_2/Bi_2MoO_6 composites exhibited an efficient performance for photocatalytic oxidation of rhodamine B under visible-light irradiation [21]. However, the mono- or few-layer heterostructured architecture of WS_2/Bi_2MoO_6 as a visual-light photocatalyst has not been reported.

Herein, we demonstrated a facile strategy to fabricate heterostructured WS_2/Bi_2MoO_6 composite via a facile solvothermal growth method using pre-exfoliated layered WS_2 nanoslices as a supporter. The WS_2/Bi_2MoO_6 exhibits excellent photocatalytic activity towards the degradation of rhodamine B (RhB) under visible-light ($\lambda > 420$ nm) irradiation. According to the microstructure characterization analysis of XRD, XPS, SEM, and TEM, the possible photocatalytic mechanism of the few-layer WS_2/Bi_2MoO_6 composite was also elucidated. It is believed that the formation of junctions between Bi_2MoO_6 and WS_2 can allow the prompt migration of photogenerated charge and reduce the self-agglomeration. It is postulated that the excellent photocatalytic activity of WS_2/Bi_2MoO_6 should be ascribed to its high migration efficiency of photo-induced carriers and the interfacial electronic interaction. These results also probably provide a valuable perspective to insight into the design of other heterostructured photocatalysts.

Methods

Preparation of the Few-Layer WS_2 Nanoslices

The liquid exfoliation of layered commercial WS_2 was accomplished following the modified report method [22]. Briefly, 50 mg commercial WS_2 powder (purchased from Aladdin Industrial Corporation) was added to 20 mL of ethanol/water with EtOH volume fractions of 40% added as dispersion solvent. The sealed flask was sonicated for 10 h, and then the dispersion was centrifuged at 3000 rpm for 20 min to remove aggregations. Finally, the supernatant was collected to obtain few-layer WS_2 nanoslices. To determine the concentrations of 2D nanosheets in the supernatant, we estimated the mass remaining in the supernatant by measuring the UV-vis absorption spectrum at fixed wavelength of 630 nm. The calculation result by virtue of Lambert–Beer Law indicated that the exfoliated WS_2 dispersion concentration was about 0.265 ± 0.02 mg/ml.

Synthesis of Hierarchical WS_2/Bi_2MoO_6 Composites

The WS_2/Bi_2MoO_6 samples were synthesized using a facile solvothermal method. Typically, 2 mmol of $Bi(NO_3)_3{\cdot}5H_2O$ was added to 10 mL of ethylene glycol solution containing dissolved $Na_2MoO_4{\cdot}2H_2O$ with the Bi/Mo molar ratio of 2:1 under magnetic stirring. An appropriate amount of exfoliated WS_2 nanoslices was dispersed into 20 mL ethanol and ultrasonicated at room temperature for 45 min. Then, it was slowly added into the above solution, followed by stirring for 10 min to form a homogeneous phase. The resulting solution was transferred into a 50-mL Teflon-lined stainless steel autoclave and kept at 160 °C for 10 h. Subsequently, the autoclave was cooled to room temperature gradually. Finally, the precipitate was centrifuged and washed with ethanol and deionized water several times and dried in a vacuum oven at 80 °C for 6 h. According to this method, WS_2/Bi_2MoO_6 composites with different WS_2 mass ratios (1, 3, 5, and 7 wt%) were synthesized. For comparison, the blank Bi_2MoO_6 was prepared in the absence of WS_2 using the same experimental conditions.

Characterization of Photocatalysts

Structure and morphology of the sample was investigated by scanning electron microscopy (SEM; JEOL JSM-6701F, Japan), transmission electron microscopy (TEM; JEOL 2100, Japan), high-resolution transmission electron microscopy (HRTEM; JEOL 2100, Japan), and powder X-ray diffraction (XRD; Bruker D8 Advance using Cu-Kα radiation source, $\lambda = 1.5406$ Å, USA). The ultraviolet-visible diffuse reflectance spectra (DRS) of samples were performed at room temperature in the range of 200–800 nm on a UV-vis spectrophotometer (Cary 500 Scan Spectrophotometers,Varian, USA) equipped with an integrating sphere attachment. The electronic states of surface elements of the catalysts were identified using X-ray photoelectron spectroscopy (XPS; Shimadzu Corporation, Japan, Al-Kα X-ray source).

Measurement of Photocatalytic Activity

In all catalytic activity of experiments, 50 mg of the samples were added to aqueous RhB solution (50 mL, 10 mg/L) magnetically stirred in a Pyrex glass vessel and then radial irradiated with a 300 W Xe arc lamp (PLS-SXE 300, Beijing Perfect Company, Labsolar-III AG) to provide visible light with $\lambda \geq 420$ nm by an ultraviolet UVCUT-420 nm cut-off filter (CE Aulight. Inc). The distance between the ultraviolet filter and aqueous RhB solution was about 6.5 mm. And the power density of visible light was 150 mW/cm^2, which was estimated by the optical power meter (PD130, Thorlabs, USA). Prior to irradiation, the suspension was kept in the dark under magnetically stirred for 30 min to ensure the establishing of an adsorption/desorption equilibrium. At given time intervals, 2 mL were collected from the suspension and immediately centrifuged; the concentration of RhB after illumination was monitored at 553 nm by using UV-vis spectrophotometer (Shimadzu UV-2550, Shimadzu Corporation, Japan). The relative concentrations (C/C_0) of the RhB were determined by the absorbance (A/A_0) at 553 nm. All experiments were carried out at least in duplicate. The reported values were within the experimental error range of ±2%. Combining with Lambert–Beer law, the photocatalytic degradation rate constant (k) of RhB was obtained using the following formula:

$$\ln(C_0/C) = kt$$

where C is RhB concentration at reaction time t, C_0 is the adsorption/desorption equilibrium concentration of RhB at the starting reaction time, and A and A_0 are the corresponding absorbance values.

In addition, to identify the active species generated during photocatalytic reactivity, various scavengers were added into the solution of RhB, including 2 mM isopropanol (IPA, a quencher of ·OH), 2 mM disodium ethylenediamine tetraacetic acid (EDTA; a quencher of h^+), and 2 mM p-benzoquinone (BQ; a $\cdot O_2^-$ scavenger), and 40 mL/min N_2 (an electron quencher). The comparative trials of photocatalytic degradation were performed under the same reaction conditions as those mentioned above.

Results and Discussion

Micostructure and Morphology Analysis

In order to confirm the composition and crystal structure of the as-prepared samples, an XRD study was carried out. As shown in Fig. 1, it can be found that the pure WS_2, five peaks located at 14.4°, 33.6°, 39.6°, 49.8°, and 58.5°, have been observed, which matched well with the (002), (101), (103), (105), and (110) crystal planes of WS_2 (JCPDS card no. 84-1398). As for the pure Bi_2MoO_6, the diffraction peaks of (131), (200), (151), (260), (331), and (262) planes at $2\theta = 28.2°$, 32.5°, 36.0°, 47.1°, 55.4°,and 58.5°, which can be indexed to orthorhombic phase of Bi_2MoO_6 (JCPDS card no. 76-2388). In the case of the few-layer WS_2/Bi_2MoO_6 composite materials, the XRD pattern only displays the characteristic diffraction peaks of hexagonal phase WS_2 and orthorhombic phase Bi_2MoO_6. Furthermore, compared with the standard data for Bi_2MoO_6 (no. 76-2388), the existence of few-layer WS_2 did not change the diffraction peak positions of Bi_2MoO_6 in the composite sample, indicating Bi_2MoO_6 nanoflakes grown on few-layer WS_2 nanoslices rather than incorporated into the WS_2 lattice. There is no trace of any impurity phase under the present resolution, which suggests the high purity of the as-prepared samples.

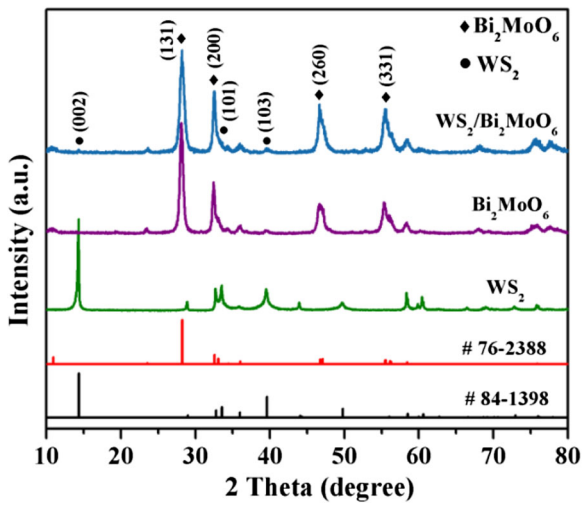

Fig. 1 X-ray diffraction patterns of Bi_2MoO_6, few-layer WS_2, and WS_2/Bi_2MoO_6 (5 wt%) composite

The morphologies of the as-synthesized samples were investigated using SEM. For comparison, SEM images of the bulk raw WS_2 without sonicated treatment and exfoliated nanoslices are shown in Fig. 2a, b. The former displays a distinct multi-layer laminated morphology with about 20 μm in thickness, while the latter exhibits 2D sheet-like morphology with thickness varying from dozens of nanometers to 1–2 μm. The results demonstrate that the layered commercial WS_2 have been stripped to few-layer WS_2 nanoslices. Figure 2c shows the SEM image of pure Bi_2MoO_6. It can be seen that the Bi_2MoO_6 exhibited microsphere morphology with rough surfaces. Closer examination reveals that the microspheres consist of numerous secondary Bi_2MoO_6 nanoplates. Furthermore, when Bi_2MoO_6 was deposited onto the 2D few-layer WS_2 via a facile solvothermal process (Fig. 2d), it can be clearly seen that the surfaces of WS_2 nanoslices were uniformly covered by numerous two-dimensional Bi_2MoO_6 nanoplates (Fig. 2d) and that formed a WS_2/Bi_2MoO_6 hierarchical structure.

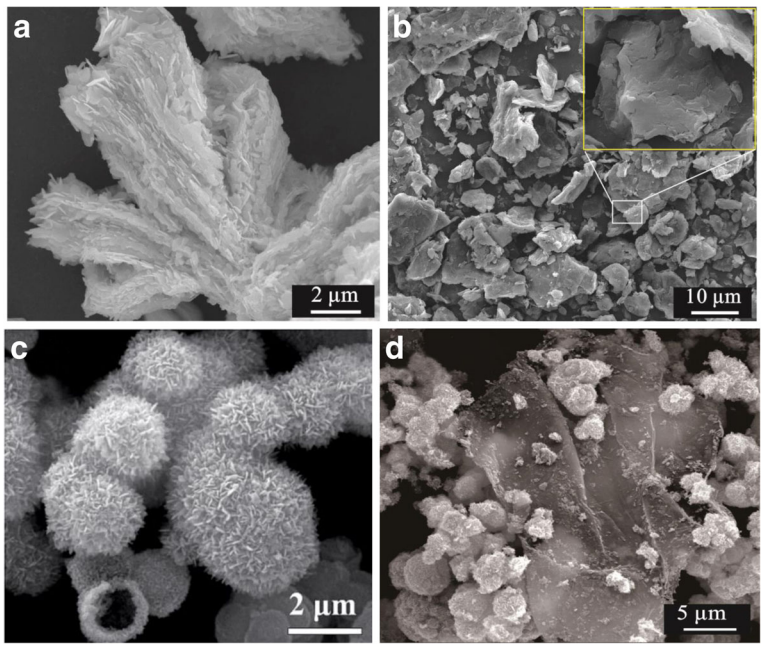

Fig. 2 SEM images of the bulk raw WS_2 (**a**), exfoliated WS_2 nanoslices (**b**), pure Bi_2MoO_6 (**c**), and WS_2/Bi_2MoO_6 (5 wt%) composite (**d**)

Further information about the nano-structure of the few-layer WS_2/Bi_2MoO_6 composites was obtained from TEM (HRTEM) images. It is easy to observe in Fig. 3a that WS_2 (purple arrows) shows a clear nanosheet structure which is similar to that of graphene, proving that graphene-like tungsten disulfide is obtained. Meanwhile, Bi_2MoO_6 nanoplates with diameters of about 50–100 nm were observed to grow on the WS_2 nanosheets. HRTEM images (Fig. 3b, c) taken from Fig. 3a clearly display the resolved lattice fringes of 0.274 and 0.227 nm, which corresponds to the (200) planes of orthorhombic phase of Bi_2MoO_6 and the (103) planes of WS_2, respectively. Therefore, the experimental results indicated that a coherent and tight heterojunction interface between few-layer WS_2 and Bi_2MoO_6 was formed, which can benefit better charge separation and efficient electron transfer within the hybrid structure in comparison with pure Bi_2MoO_6.

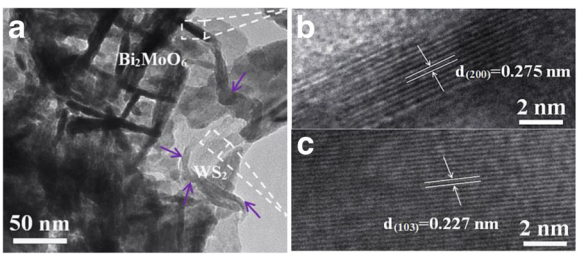

Fig. 3 TEM (**a**) and HRTEM (**b**, **c**) images of WS_2/Bi_2MoO_6 (5 wt%) composite

Electronic Structure and Spectrum Analysis

The elemental composition and oxidation states of the fewlayer WS_2/Bi_2MoO_6 composites were further determined by XPS spectra. Figure 4a shows the survey XPS spectra of the few-layer WS_2/Bi_2MoO_6 (5 wt%) sample, which exhibits W, S, O, Bi, Mo, and C peaks. No peaks corresponding to other elements are observed. The peak for Bi 4f in the Bi_2MoO_6 (Fig. 4b) which appeared at 164.4 and 159.2 eV belonged to Bi $4f_{5/2}$ and Bi $4f_{7/2}$ of Bi^{3+} ions [23]. The Mo 3d binding energy (Fig. 4c) of 235.6 and 232.5 eV is consistent with the Mo $3d_{3/2}$ and Mo $3d_{5/2}$ of Mo^{4+} ions [23]. The asymmetric peaks of O 1 s (Fig. 4d) are located at 530.0 eV, which are characteristic of the Mo-O [24]. However, the binding energies of Bi 4f, Mo 3d, and O 1 s in the XPS spectra (Fig. 4b–d) of the hierarchical WS_2/Bi_2MoO_6 slightly shift (about 0.2 eV) toward lower binding energies as compared with the pure Bi_2MoO_6. Meanwhile, in the hierarchical WS_2/Bi_2MoO_6 composite, the values of W $4f_{5/2}$ (34.2 eV) and W $4f_{7/2}$ (32.0 eV) peaks (Fig. 4e) corresponding to WS_2 are slightly lower (about 0.2 eV) than the pure WS_2 (34.4 and 32.2 eV). Similarly, the high-resolution S 2p spectrum (Fig. 4f) also slightly shifts toward lower binding energies of 0.3 eV. These results could be ascribed to the strong interaction between WS_2 and Bi_2MoO_6 resulting in an inner shift of Bi 4f, Mo 3d, O 1 s W 4f, and S 2p orbits [21, 25]. Therefore, by combining the XRD, SEM, TEM, and XPS investigations, it revealed that there are both WS_2 and Bi_2MoO_6 species in the hierarchical WS_2/Bi_2MoO_6 composite and that the heterojunctions are formed in their contact interface.

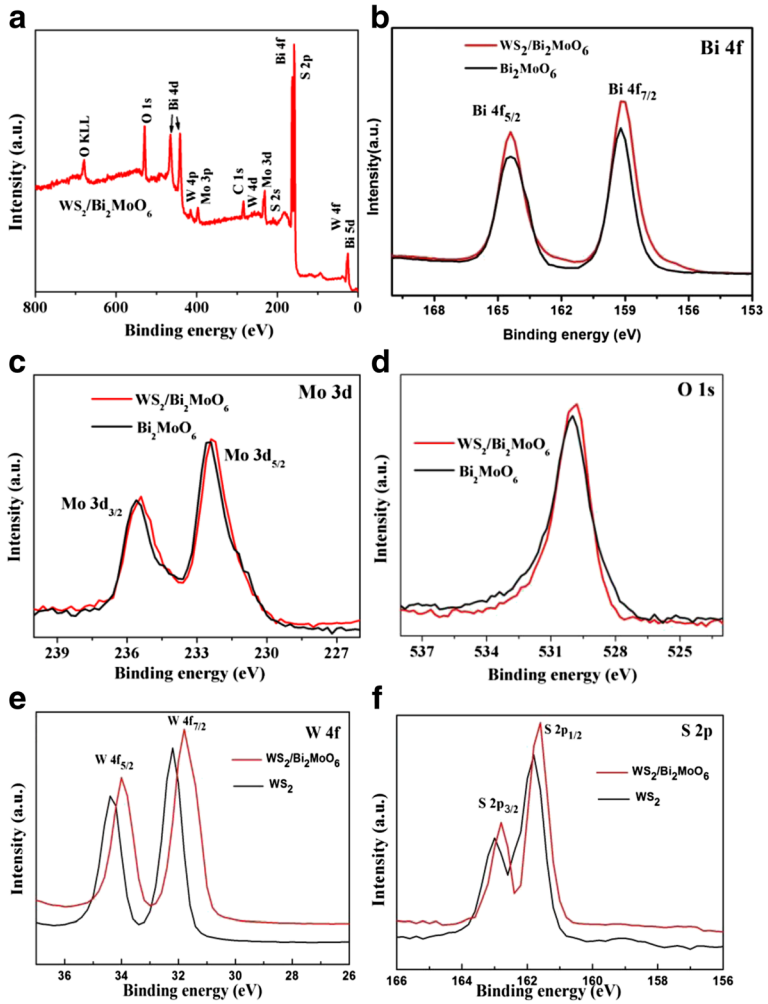

Fig. 4 Survey XPS spectra of the WS_2/Bi_2MoO_6 composite (**a**) and the high-resolution XPS spectra of Bi 4f (**b**), Mo 3d (**c**), O 1 s (**d**), W 4f (**e**), and S 2p (**f**) from Bi_2MoO_6, WS_2, and the WS_2/Bi_2MoO_6 composite (5 wt%)

Figure 5a shows a comparison of the UV-vis diffuse reflectance spectra (UV-Vis-DRS) of the WS_2, Bi_2MoO_6 and hierarchical WS_2/Bi_2MoO_6 composite with different WS_2 contents. It can be clearly seen that the absorption spectrum of pure Bi_2MoO_6 extends from the UV region to visible light at about 450 nm. When WS_2 combined with Bi_2MoO_6, the absorption spectrum of the hierarchical composite exhibits an obviously redshift and more intensive absorption within the visible-light range in comparison with pure Bi_2MoO_6. Meanwhile, when the content of WS_2 increased to a relatively high (3 to 7 wt%), the hierarchical composite display surprisingly strong absorption around 450–800 nm. These results clearly indicate that the composite photocatalyst could absorb more photons during photocatalytic reaction. Therefore, it can be revealed that the addition of WS_2 nanoslices is beneficial for the visible-light absorbance of the WS_2/Bi_2MoO_6 composite.

In addition, the optical band gap energies (E_g) of samples were calculated by the following equation [26]:

$$\alpha h\nu = A\left(h\nu - E_g\right)^{n/2}$$

where α, $h\nu$, A, and E_g are absorption coefficient, photon energy, proportionality constant, and bandgap, respectively. The value of n is determined by the type of transition (direct ($n = 1$) or indirect ($n = 4$)) [27, 28]. A plot of $(ahv)^2$ versus (hv) is converted according the UV-Vis-DRS. As shown in Fig. 5b, the E_g values of pure WS_2 and Bi_2MoO_6 have been estimated to be 1.47 and 2.72 eV, respectively.

Photocatalytic Activity

The photocatalytic activities of the as-prepared samples were measured by degrading rhodamine B (RhB) under

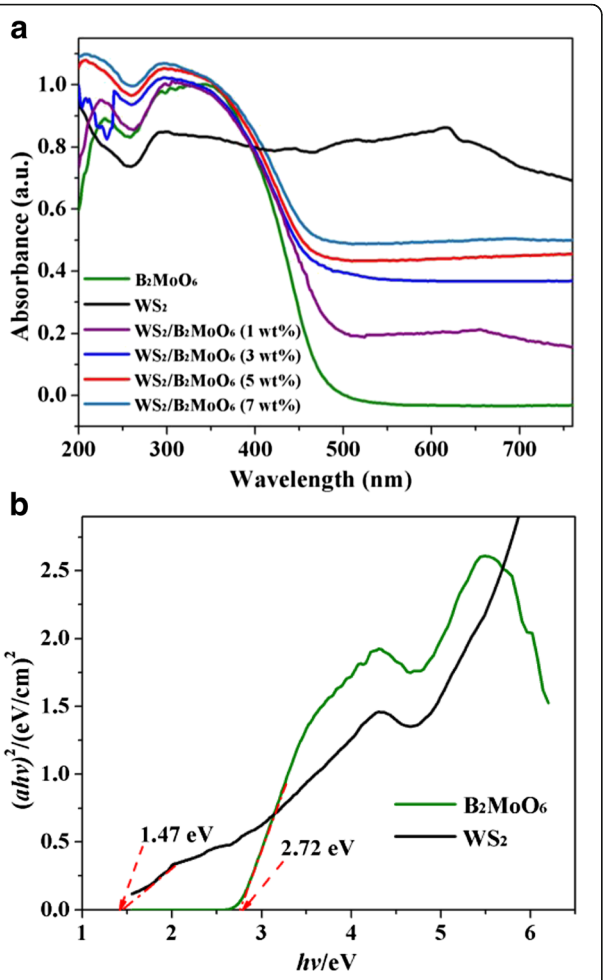

Fig. 5 **a** UV-vis diffuse reflectance spectra (UV-Vis-DRS) of the as-prepared samples. **b** Plot of the transformed Kubelka–Munk functions vs. the energy of light

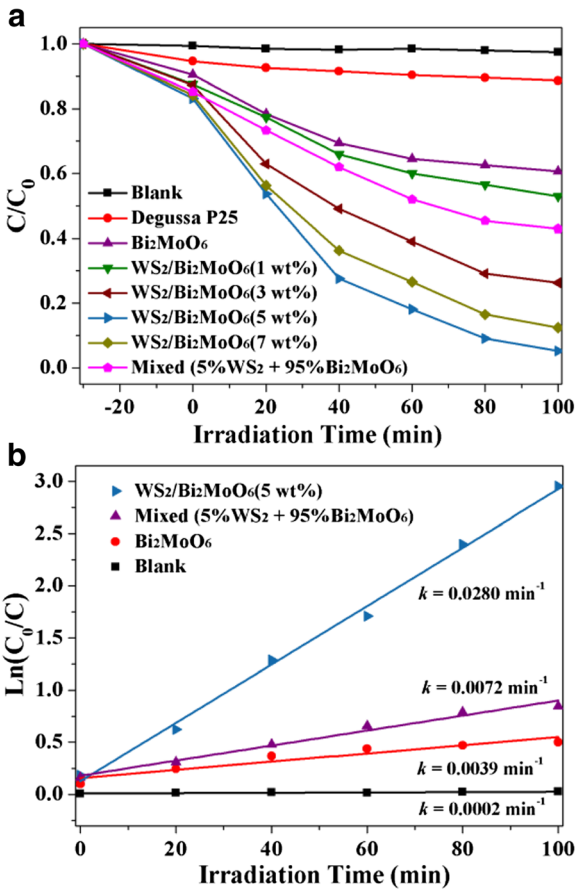

Fig. 6 The photocatalytic activity (**a**) and kinetic fit (**b**) of the different photocatalysts for RhB degradation

visible-light irradiation. For comparison, photocatalytic activities of pure Bi_2MoO_6 and mechanically mixed samples (5% WS_2 and 95% Bi_2MoO_6) have also been investigated. As shown in Fig. 6a, the self-degradation effect of RhB under visible-light irradiation could be ignored. It can be clearly seen that the photodegradation rate of RhB by the pure Bi_2MoO_6 was only ~39% after 100 min of visible-light irradiation. Obviously, all the hierarchical WS_2/Bi_2MoO_6 composites show better photocatalytic performance than the pure Bi_2MoO_6. ~48, ~74, ~95, and ~88% of RhB were degraded using 1% WS_2/Bi_2MoO_6, 3% WS_2/Bi_2MoO_6, 5% WS_2/Bi_2MoO_6, and 7% WS_2/Bi_2MoO_6, respectively. The results indicate that the optimal WS_2 content in WS_2/Bi_2MoO_6 composite exists when the mass ratio is 5%. Meanwhile, it was noted that the WS_2/Bi_2MoO_6 (5 wt%) composite exhibits remarkably superior photocatalytic activity than the mechanically mixed 5% WS_2 and 95% Bi_2MoO_6. This strongly suggests that an effective nanojunction interface contact and strong interactions between WS_2 and Bi_2MoO_6 are extremely useful to enhance the migration, transport, and separation processes of photogenerated carriers. Furthermore, such superior photocatalytic performances could be attributed to the good crystallization and high specific surface area of composites and the small sheet thickness of the WS_2 substrate.

In addition, the pseudo-first-order kinetics model was used to fit the experimental data of the photocatalytic degradation of the RhB solution, and the results are given in Fig. 6b. The rate constant k is 0.0280 min^{-1} for the hierarchical WS_2/Bi_2MoO_6 (5 wt%) composites, which is 3.8 and 7.1 times greater than those of mechanically mixed WS_2 and Bi_2MoO_6 and pure Bi_2MoO_6, respectively. These results indicated that RhB could be degraded more efficiently by the hierarchical WS_2/Bi_2MoO_6 composite photocatalyst.

Figure 7 shows the UV-vis adsorption spectra changes of RhB solution degradation over the WS_2/Bi_2MoO_6 (5 wt%) composite photocatalyst, which was performed to further study the photocatalytic degradation process of RhB. It can be seen that the main absorption peak of

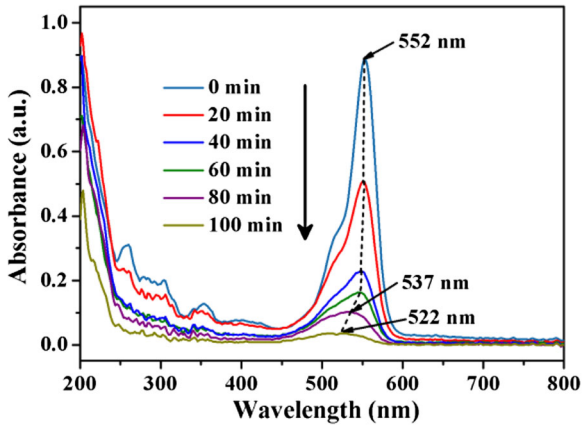

Fig. 7 The optical adsorption spectra changes of RhB solution degradation over the WS_2/Bi_2MoO_6 composite (5 wt%)

RhB gradually shifted from 552 to 537 nm, corresponding to the stepwise formation of a series of *N*-de-ethylated intermediates. As the visible-light irradiation process continues, the peak located at 537 nm is continued to shift and decrease, which indicates that the RhB molecules were further decomposed into smaller molecular fragments and the structure of RhB was also destroyed in the end. The two-step transition processes for photodegradation of RhB were also reported in several previous studies [29, 30]. Meanwhile, the suspension loses color gradually in the experiment, which further indicates that the structure of RhB has been destroyed in the end.

Catalyst Stability

The photocatalytic stability of the hierarchical WS_2/Bi_2MoO_6 composites was investigated by repeatability experiments for degradation of RhB, as shown in Fig. 8a. It can be found that the photocatalytic activity of WS_2/Bi_2MoO_6 remains stable in the first two-cycle experiments. After four recycles, the catalysts did not show an obvious decrease in photocatalytic activity, demonstrating that WS_2/Bi_2MoO_6 composite retained a relatively high degradation activity during the photodegradation process. Furthermore, the catalyst samples collected after four cycles was characterized by XRD measurement (Fig. 8b). It can be seen that the crystal structure and phase composition of WS_2/Bi_2MoO_6 composite do not change after four photocatalytic reactions. Thus, the good structural stability ensures the WS_2/Bi_2MoO_6 composite efficient photocatalysts working under visible-light irradiation.

Possible Photocatalytic Mechanism

Figure 9 shows the trapping experiment of main active species in the photocatalytic process of the WS_2/Bi_2MoO_6 composite. Isopropanol (IPA), 1,4-benzoquinone (BQ), and

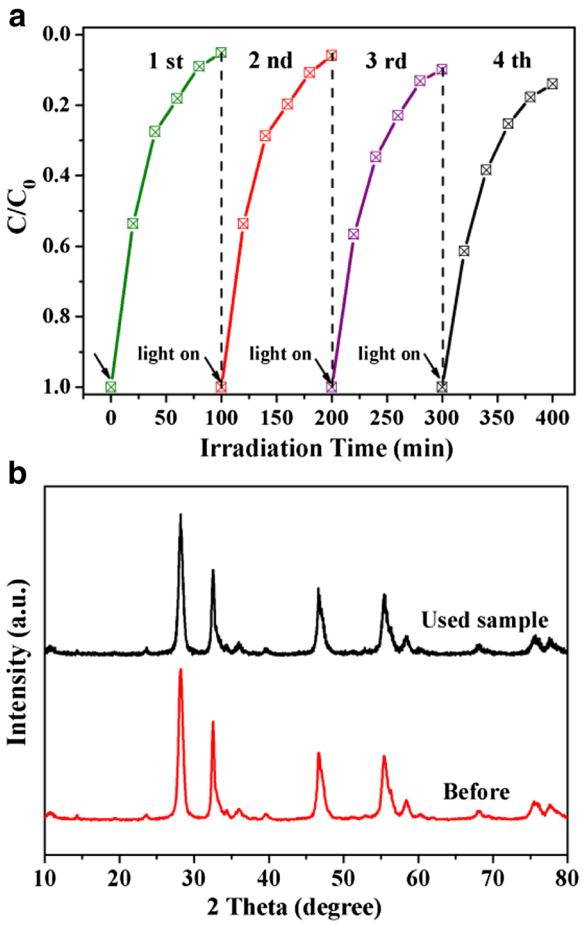

Fig. 8 **a** Cycling runs for degradation of RhB over the WS_2/Bi_2MoO_6 composite (5 wt%) under visible-light irradiation. **b** XRD patterns of the the WS_2/Bi_2MoO_6 sample before and after four-cycle experiments

disodium ethylenediamine tetraacetic acid (EDTA) acted as the scavengers for ·OH, $\cdot O_2^-$, and h^+, respectively. It can be observed that the addition of 2 mM IPA or BQ in the RhB solution had a little effect on the rate constant k_{app}, suggesting that ·OH and $\cdot O_2^-$ are the secondary active species during the photocatalytic reaction, not the main active species during the photocatalytic reaction. On the contrary, the k_{app} for degradation of RhB obviously decreased after the addition of 2 mM EDTA. Therefore, it can be confirmed that h^+ play a key role for degradation of RhB. Furthermore, N_2 was bubbled into the RhB solution at the rate of 40 mL/min to ensure that the reaction was operated without O_2 as an electron quencher. The degradation of RhB showed a slight decrease in comparison with the case of the air-equilibrated solution and further indicated that $\cdot O_2^-$ played a minor role.

To explain the enhanced photocatalytic performance, conduction band (CB) and valence band (VB) of WS_2 and Bi_2MoO_6 potentials should be calculated. For a semiconductor, the bottom CB and top VB can be estimated by

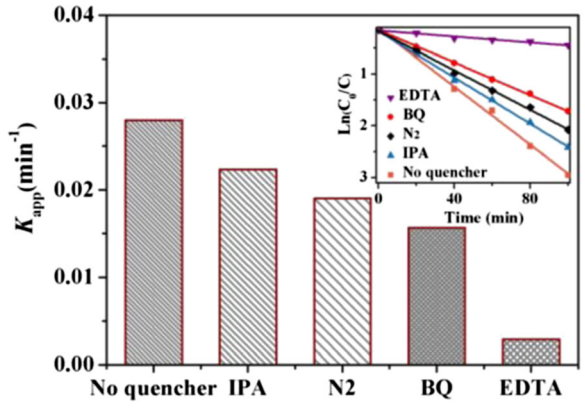

Fig. 9 Rate constant k_{app} of the WS_2/Bi_2MoO_6 (5 wt%) composite for the degradation of RhB in the presence of different scavengers under visible-light irradiation

the empirical formula [31]: $E_{CB} = X - E_0 - 0.5E_g$ and $E_{VB} = E_{CB} + E_g$, where E_{CB} (E_{VB}) is the CB (VB) edge potential; X is the electronegativity of the semiconductor; E_0 is the energy of free electrons of the hydrogenscale (~4.5 eV *vs* NHE); and E_g is the band gap energy of the semiconductor obtained from the UV-visible diffuse reflectance absorption. The X values for WS_2 and Bi_2MoO_6 are calculated to be 5.66 and 5.55 eV, respectively [28, 32, 33]. Thus, E_{CB} and E_{VB} values of WS_2 are determined to be +0.43 and +1.9 eV and Bi_2MoO_6 are −0.31 and +2.41 eV, respectively.

On the basis of the above results, a possible photocatalytic mechanism scheme of the WS_2/Bi_2MoO_6 composite photocatalyst is shown in Fig. 10. It can be found that WS_2 and Bi_2MoO_6 are excited under visible-light irradiation and generate electrons and holes in their CB and VB, respectively. The electrons on CB of Bi_2MoO_6 will easily transfer WS_2 due to the CB potential of Bi_2MoO_6 (−0.31 eV) is more negative than the CB potential of WS_2 (0.43 eV) [29, 30]. The few-layer WS_2 nanoslices could act as effective electron collectors, which was favorable to the separation of electron–hole pairs in Bi_2MoO_6. Therefore, this fast electron and hole transfer process can decrease the recombination of charges and prolong the lifetime of holes on VB of Bi_2MoO_6 [34]. The CB potential of WS_2 (+0.43 eV) is more positive than E_0 ($O_2/\cdot O_2^-$) (−0.046 eV) which suggests that the $\cdot O_2^-$ radicals were not formed through electrons reducing the dissolved O_2 [35]. However, a few electrons on the CB of Bi_2MoO_6 can react with dissolved O_2 to yield $\cdot O_2^-$ radicals because its potential (−0.31 eV) is more negative than E_0 ($O_2/\cdot O_2^-$). Thus, the $\cdot O_2^-$ active species played a minor role. Meanwhile, the photo-induced holes on VB of Bi_2MoO_6 could not also directly oxidize the adsorbed H_2O molecules to ·OH radicals because its potential (+2.41 eV) was lower than E_0 (·OH/H_2O) (+2.68 V) [36]. Finally, the main active species holes and minor active species $\cdot O_2^-$ act as a strong oxidizing agent to oxidize the organic pollutants (RhB) to CO_2 and H_2O. Therefore, the hierarchical WS_2/Bi_2MoO_6 composites exhibit improved photocatalytic activity.

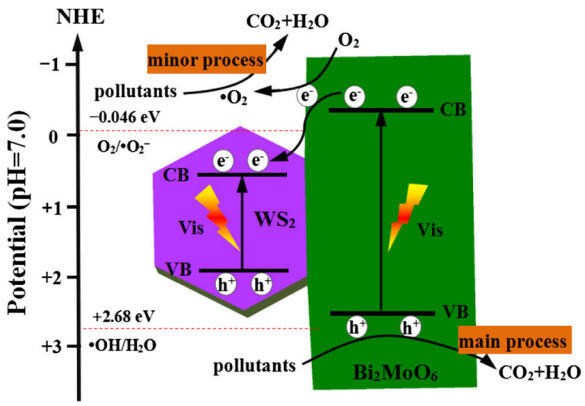

Fig. 10 The proposed photocatalytic mechanism scheme of WS_2/Bi_2MoO_6 composite under visible light (>420 nm)

Conclusions

In summary, a novel WS_2/Bi_2MoO_6 heterostructured photocatalysts were successfully fabricated via a facile solvothermal growth method using pre-exfoliated layered WS_2 nanoslices as a substrate. The hierarchical WS_2/Bi_2MoO_6 exhibits excellent photocatalytic activity towards the degradation of rhodamine B (RhB) under visible-light irradiation. Based on the results of a series of structure and performance tests, it is believed that there formed a tight nanojunction interface between layered WS_2 nanoslices and Bi_2MoO_6 nanoflakes, which make the photo-induced electrons be easily transferred to the WS_2 substrate. As a result, the recombination of charges was decreased and the lifetime of holes was prolonged. Therefore, the hierarchical WS_2/Bi_2MoO_6 composites exhibit much higher visible-light-driven photocatalytic activity than the pure Bi_2MoO_6. Furthermore, the WS_2/Bi_2MoO_6 composites are very stable under visible-light irradiation and cycling photocatalytic tests. Thus, the as-prepared WS_2/Bi_2MoO_6 photocatalyst has potential application for pollutant abatement.

Acknowledgements

The authors genuinely appreciate the financial support of this work by the National Natural Science Foundation of China (No. 51568068, No. 51568067).

Authors' Contributions

JG carried out the sample preparation and experimental measurements and drafted the manuscript. CL and FW conceived the work, supervised the experiments, and revised the manuscript. LJ and KD helped to analyze the characterization results. TL supervised all of the study and provided financial support. All authors read and approved the final manuscript.

Competing Interests
The authors declare that they have no competing interests.

Publisher's Note

Author details
[1]Joint Research Centre for International Cross-border Ethnic Regions Biomass Clean Utilization in Yunnan, Kunming 650500, China. [2]Education Department of Yunnan, Key Laboratory of Resource Clean Conversion in Ethnic Region, Kunming 650500, China. [3]Key Laboratory of Comprehensive Utilization of Mineral Resources in Ethnic Regions, Kunming 650500, China. [4]College of Chemistry and Environment, Yunnan MinZu University, Kunming 650500, China.

Received: 29 March 2017 Accepted: 19 May 2017
Published online: 30 May 2017

References

1. Fujishima A, Honda K (1972) Photolysis-decomposition of water at the surface of an irradiated semiconductor [J]. Nature 238(5385):37–38
2. Linsebigler AL, Lu GQ, Yates JT (1995) Interfacial photochemistry, fundamentals and applications [J]. Chem Rev 95(3):735–758
3. Xia Y, Yang P, Sun Y et al (2003) One-dimensional nanostructures: synthesis, characterization, and applications [J]. Adv Mater 15(5):353–389
4. Sang Y, Liu H, Umar A (2015) Photocatalysis from UV/Vis to near-infrared light: towards full solar light spectrum activity [J]. Chem Catal Chem 7(4):559–573
5. Zhang Z, Wang W, Wang L et al (2015) Enhancement of visible-light photocatalysis by coupling with narrow-band-gap semiconductor: a case study on Bi_2S_3/Bi_2WO_6 [J]. ACS Appl Mater Interfaces 4(2):593
6. Guo S, Bao J, Hu T et al (2015) Controllable synthesis porous Ag_2CO_3 nanorods for efficient photocatalysis [J]. Nanoscale Res Lett 10(1):1–8
7. He W, Kim HK, Wamer WG et al (2014) Photogenerated charge carriers and reactive oxygen species in ZnO/Au hybrid nanostructures with enhanced photocatalytic and antibacterial activity [J]. J Am Chem Soc 136(2):750
8. Wang H, Zhang L, Chen Z et al (2014) Semiconductor heterojunction photocatalysts: design, construction, and photocatalytic performances [J]. Chem Soc Rev 43(15):5234–5244
9. Bao J, Guo S, Gao J et al (2015) Synthesis of Ag_2CO_3/Bi_2WO_6 heterojunctions with enhanced photocatalytic activity and cycling stability [J]. RSC Adv 5(118): 97195–97204
10. Yin W, Wang W, Sun S (2010) Photocatalytic degradation of phenol over cage-like Bi_2MoO_6 hollow spheres under visible-light irradiation [J]. Catal Comm 11(7):647–650
11. Yue D, Chen D, Wang Z et al (2014) Enhancement of visible photocatalytic performances of a Bi_2MoO_6-BiOCl nanocomposite with plate-on-plate heterojunction structure [J]. Phys Chem Chem Phys 16(47):26314–26321
12. Wang QH, Kalantarzadeh K, Kis A et al (2012) Electronics and optoelectronics of two-dimensional transition metal dichalcogenides [J]. Nat Nanotechnol 7(11):699–712
13. Xu M, Liang T, Shi M et al (2013) Graphene-like two-dimensional materials [J]. Chem Rev 113(5):3766–3798
14. Chhowalla M, Shin HS, Eda G et al (2013) The chemistry of two-dimensional layered transition metal dichalcogenide nanosheets [J]. Nature Chem 5(4):263–275
15. Geim AK, Novoselov KS (2007) The rise of graphene [J]. Nature Mater 6(3):183–191
16. Albe K, Klein A (2002) Density-functional-theory calculations of electronic band structure of single-crystal and single-layer WS_2 [J]. Phys Rev B 66(7):73413
17. Visic B, Dominko R, Gunde MK et al (2011) Optical properties of exfoliated MoS_2 coaxial nanotubes analogues of graphene [J]. Nanoscale Res Lett 6(1):593
18. Coehoorn R, Haas C, Dijkstra J et al (1987) Electronic structure of $MoSe_2$, MoS_2, and WSe_2. Band-structure calculations and photoelectron spectroscopy [J]. Phys Rev B 35(12):6195
19. Li Q, Zhang N, Yang Y et al (2014) High efficiency photocatalysis for pollutant degradation with MoS_2/C_3N_4 heterostructures [J]. Langmuir 30(29):8965
20. Shi J, Tong R, Zhou X et al (2016) Temperature-Mediated selective growth of MoS_2/WS_2 and WS_2/MoS_2 vertical stacks on Au foils for direct photocatalytic applications [J]. Adv Mater 28(48):10664
21. Chen Y, Tian G, Shi Y et al (2015) Hierarchical MoS_2/Bi_2 MoO_6 composites with synergistic effect for enhanced visible photocatalytic activity [J]. Appl Catal B: Environmental 164:40–47
22. Zhou K, Mao N, Wang H et al (2011) A mixed-solvent strategy for efficient exfoliation of inorganic graphene analogues [J]. Angew Chem Int Ed 50(46): 10839–10842
23. Tian G, Chen Y, Zhou J et al (2014) In situ growth of Bi_2MoO_6 on reduced graphene oxide nanosheets for improved visible-light photocatalytic activity [J]. Crystengcomm 16(5):842
24. Li H, Liu J, Hou W et al (2014) Synthesis and characterization of g-C_3N_4/Bi_2MoO_6 heterojunctions with enhanced visible light photocatalytic activity [J]. Appl Catal B: Environmental 160(1):89–97
25. Yan T, Yan Q, Wang X et al (2015) Facile fabrication of heterostructured g-C_3N_4/Bi_2MoO_6 microspheres with highly efficient activity under visible light irradiation [J]. Dalton T 44(4):1601–1611
26. Wu D, Long M (2011) Realizing visible-light-induced self-cleaning property of cotton through coating N-TiO_2 film and loading AgI particles [J]. ACS Appl Mater Interfaces 3(12):4770
27. Long J, Wang S, Chang H et al (2014) Bi_2MoO_6 nanobelts for crystal facet-enhanced photocatalysis [J]. Small 10(14):2791–2795
28. Yu H, Yu Y, Liu J et al (2015) Space-confined growth of Ag_3PO_4 nanoparticles within WS_2 sheets: Ag_3PO_4/WS_2 composites as visible-light-driven photocatalysts for decomposing dyes [J]. J Mater Chem A 3(38):19439–19444
29. Cheng Z, Wang Z, Shifa TA et al (2015) Au plasmonics in a WS_2-Au-$CuInS_2$ photocatalyst for significantly enhanced hydrogen generation [J]. Appl Phys Lett 107(22):223902
30. Chen G, Li F, Fan Y et al (2013) A novel noble metal-free ZnS-WS_2/CdS composite photocatalyst for H_2 evolution under visible light irradiation [J]. Catal Comm 40(19):51–54
31. Zhang X, Zhang L, Xie T et al (2009) Low-temperature synthesis and high visible-light-induced photocatalytic activity of BiOI/TiO_2 heterostructures [J]. J Phys Chem C 113(17):7371–7378
32. Sang Y, Zhao Z, Zhao M et al (2014) From UV to near-infrared, WS_2 nanosheet: a novel photocatalyst for full solar light spectrum photodegradation [J]. Adv Mater 27(2):363–369
33. Xu Y, Zhang W (2012) Monodispersed Ag_3PO_4 nanocrystals loaded on the surface of spherical Bi_2MoO_6 with enhanced photocatalytic performance [J]. Dalton T 42(4):1094–1101
34. Huo N, Yue Q, Yang J et al (2013) Abnormal photocurrent response and enhanced photocatalytic activity induced by charge transfer between WS_2 nanosheets and WO_3 nanoparticles [J]. Chem phys chem 14(18):4069–4073
35. Ye L, Liu J, Gong C et al (2012) Two different roles of metallic Ag on Ag/AgX/BiOX (X = Cl, Br) visible light photocatalysts: surface plasmon resonance and Z-scheme bridge [J]. Acs Catalysis 2(8):1677–1683
36. Song Y, Lei Y, Xu H et al (2015) Synthesis of few-layer MoS_2 nanosheet-loaded Ag_3PO_4 for enhanced photocatalytic activity [J]. Dalton Trans 44(7):3057–3066